Available online at www.sciencedirect.com

SCIENCE DIRECT®

International Journal of Heat and Mass Transfer 47 (2004) 4061–4073

International Journal of HEAT and MASS TRANSFER

www.elsevier.com/locate/ijhmt

Flow pattern evolution in natural convection cooling from an array of discrete heat sources in a rectangular cavity at various orientations

C.P. Tso [a,b,*], L.F. Jin [a], S.K.W. Tou [a], X.F. Zhang [a]

[a] *School of Mechanical and Production Engineering, Nanyang Technological University, 50 Nanyang Avenue, Singapore 639798, Singapore*

[b] *Faculty of Engineering and Technology, Multimedia University, Jalan Ayer Keroh Lama, 75450 Melaka, Malaysia*

Received 7 November 2003; received in revised form 27 May 2004

Abstract

Experimental data are presented for laminar natural convection cooling of water in a rectangular cavity with a 3×3 array of heaters on one wall, and the cavity at various inclined angles. Generally, heaters in the same row have close temperatures, due to weak velocity in the horizontal direction. Numerical simulations in 2-D and 3-D are also reported, showing flow and temperature pattern evolution at different inclined angles. In particular, the case of horizontal cavity heated from below reveals flow fields of the toroidal, bimodal or Rayleigh–Benard convection type, depending on the Rayleigh number, and this is also the most desirable orientation for heat transfer. When the enclosure is inclined toward the horizontal orientation (heated from below), the flow and temperature fields become complex and distorted.

1. Introduction

With the advent of electronics cooling, researchers begin to study natural convection cooling from an array of discrete heat sources in the vertical enclosure [1–12]. The problem of discrete heat sources attached to an inclined or horizontal surface of an electronic package is widely encountered in the industry. However, studies in these fields are considerably limited [13,14]. One challenge from numerical simulations is that around horizontal orientation, the field is essentially of the Rayleigh–Benard (henceforth referred to as R–B) type. The evolution of R–B convection from stable bimodal convection to unstable convection is reported by Mukutmoni and Yang [15] in the container with constant hot and cold wall temperature. This motivates the present study to investigate the complex interactions of thermal and internal fluid flow fields from an array of discrete heat sources in an inclined rectangular cavity. Experimental data are presented first and they are used to validate the numerical simulations, extending earlier work [12,16]. Then flow pattern and temperature contours at different inclination angles are garnered as greater details are available from the numerical analysis. Since there is also interest to develop and test new coolants with different Prandtl number (*Pr*), we also discuss the role of *Pr* in the present investigation in inclined orientations, which has not been reported before.

2. Model formulation

The geometrical and physical model to be considered in this study is depicted schematically in Fig. 1 and Table 1. A three-dimensional Cartesian coordinate system is selected such that the *z*-axis points positively upwards while the gravitational force acts downwards.

---

[*] Corresponding author. Address: Faculty of Engineering and Technology, Multimedia University, Jalan Ayer Keroh Lama, 75450 Melaka, Malaysia.

E-mail address: cptso@mmu.edu.my (C.P. Tso).

0017-9310/$ - see front matter © 2004 Elsevier Ltd. All rights reserved.
doi:10.1016/j.ijheatmasstransfer.2004.05.022

Nomenclature

A_h	heat source area (m^2)
g	magnitude of gravitational acceleration (m^2/s)
H	the side of the enclosure (m)
H_1, H_3	enclosure heater location (m)
i	row number of heaters
k	thermal conductivity (W/m K)
L	enclosure along the x-direction (m)
L_1, L_3	enclosure heater location (m)
L_x	thermal diffusivity (m^2/s)
L_x	heater length in x-direction (m)
L_z	heater length in z-direction (m)
Nu, $\overline{Nu}$, $\overline{\overline{Nu}}$	local, row averaged and overall mean Nusselt number
p	pressure (Pa)
p_m	motion pressure (Pa)
P_m	dimensionless motion pressure
Pr	Prandtl number
P_x	heater pith in the x-direction (m)
P_z	heater pith in the x-direction (m)
q''	heat flux (W/m^2)
q'''	heat generation density (W/m^3)
Ra, Ra^*	Rayleigh number and modified Rayleigh number
T	temperature (K)
T_c	temperature of the cold wall (K)
u, v, w	dimensional velocity components (m/s)
U, V, W	dimensionless velocity components
$\vec{V}$	dimensionless velocity vector
W	enclosure width (m)
W_1, W_3	enclosure heater location (m)
x, y, z	dimensional Cartesian coordinate system (m)
X, Y, Z	dimensionless Cartesian coordinate system
Greek symbols	
α	thermal diffusivity (m^2/s)
β	thermal expansion coefficient (K^{-1})
θ	dimensionless temperature
ν	fluid kinematic viscosity (m^2/s)
ρ	density at the mean temperature (kg/m^3)
ϕ	angular position of cavity (°)

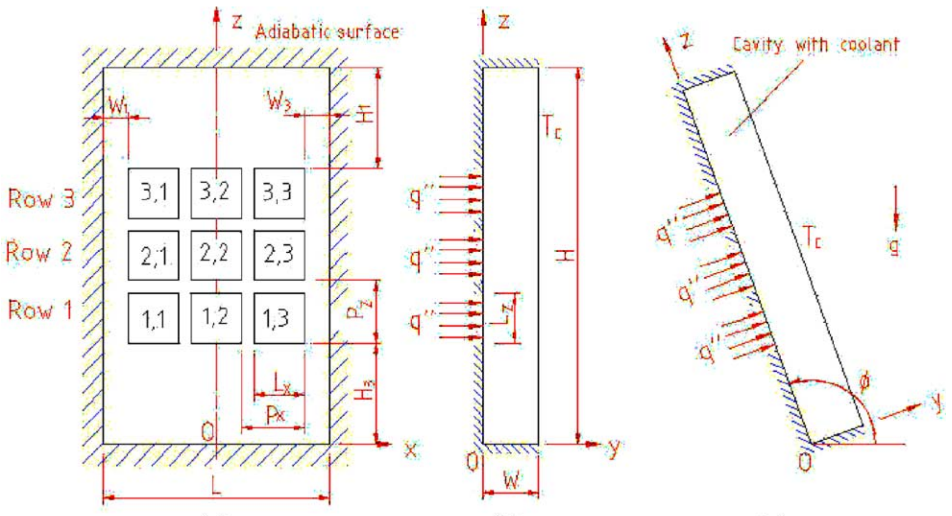

Fig. 1. Physical configuration, boundary conditions and the coordinate system: (a) heaters position; (b) side view; (c) inclined position.

The enclosure, filled with liquid, can be rotated about the horizontal X-axis to alter its configuration set by the angle of inclination. An array of 3×3 discrete heat sources is flush-mounted onto one of the sidewalls, while the opposite wall acts as a uniform cold surface. The remaining walls are insulated from surroundings.

2.1. Governing equations

In three-dimension, the governing equations are:
Continuity equation

$$\frac{\partial U}{\partial X}+\frac{\partial V}{\partial Y}+\frac{\partial W}{\partial Z}=0. \tag{1}$$

Table 1
Summary on geometric parameters

(a) Fixed geometric parameters $H = 95.3$ mm, $L = 57.2$ mm, $L_z = 12.7$ mm, $W = 12.7$ mm								
H/L_z	L/L_z	L_x/L_z	P_x/L_z	P_z/L_z	H_1/L_z	H_3L_z	W_1/L_z	W_3/L_z
7.5	4.5	1	1.25	1.25	2.0	2.0	0.5	0.5
(b) Variable geometric parameter								
$\phi = 0$–180°, at 5° intervals (2-D model)								
$\phi = 0°, 30°, 45°, 60°, 90°, 120°, 135°, 150°, 180°$ (3-D model)								

X-momentum equation

$$U\frac{\partial U}{\partial X}+V\frac{\partial U}{\partial Y}+W\frac{\partial U}{\partial Z} = -\frac{\partial P_m}{\partial X}+Pr\left[\frac{\partial^2 U}{\partial X^2}+\frac{\partial^2 U}{\partial Y^2}+\frac{\partial^2 U}{\partial Z^2}\right]. \tag{2}$$

Y-momentum equation

$$U\frac{\partial V}{\partial X}+V\frac{\partial V}{\partial Y}+W\frac{\partial V}{\partial Z} = -\frac{\partial P_m}{\partial Y}+Pr\left[\frac{\partial^2 V}{\partial X^2}+\frac{\partial^2 V}{\partial Y^2}+\frac{\partial^2 V}{\partial Z^2}\right]+Ra^*Pr\theta\sin\phi. \tag{3}$$

Z-momentum equation

$$U\frac{\partial W}{\partial X}+V\frac{\partial W}{\partial Y}+W\frac{\partial W}{\partial Z} = -\frac{\partial P_m}{\partial Z}+Pr\left[\frac{\partial^2 W}{\partial X^2}+\frac{\partial^2 W}{\partial Y^2}+\frac{\partial^2 W}{\partial Z^2}\right]+Ra^*Pr\theta\cos\phi. \tag{4}$$

Energy equation

$$U\frac{\partial \theta}{\partial X}+V\frac{\partial \theta}{\partial Y}+W\frac{\partial \theta}{\partial Z}=\frac{\partial^2 \theta}{\partial X^2}+\frac{\partial^2 \theta}{\partial Y^2}+\frac{\partial^2 \theta}{\partial Z^2}. \tag{5}$$

In the above, P_m is the dimensionless pressure defined as $P_m = p_m L_z^2/(\alpha^2\rho)$ and p_m is the motion pressure and defined as

$$p_m = p + \rho g y\sin\phi + \rho g z\cos\phi. \tag{6}$$

Thus,

$$-\frac{\partial p_m}{\partial x} = -\frac{\partial p}{\partial x}, \tag{7}$$

$$-\frac{\partial p_m}{\partial y} = -\frac{\partial p}{\partial y} - \rho g\sin\phi, \tag{8}$$

$$-\frac{\partial p_m}{\partial z} = -\frac{\partial p}{\partial z} - \rho g\cos\phi. \tag{9}$$

Other dimensionless parameters are:

$$\left.\begin{aligned} &X = x/L_z, \quad Y = y/L_z, \quad Z = z/L_z,\\ &U = uL_z/\alpha, \quad V = vL_z/\alpha, \quad W = wL_z/\alpha,\\ &Ra^* = gq''L_z^4\beta/(k\nu\alpha), \quad \theta = k(T-T_c)/(q''L_z). \end{aligned}\right\} \tag{10}$$

The local Nusselt number (Nu), row averaged Nusselt number ($\overline{Nu}$), and overall mean Nusselt number ($\overline{\overline{Nu}}$) are defined below:

$$\left.\begin{aligned} &Nu(X,Z) = \frac{qL_z}{(T(X,Z)|_{Y=0}-T_c)k} = \frac{1}{\theta|_{Y=0}},\\ &\overline{Nu_i} = \frac{1}{\frac{1}{A_h}\int_{A_h}\theta|_{Y=0}\mathrm{d}A_h}, \quad (i=1,2,3),\\ &\overline{\overline{Nu}} = \left(\textstyle\sum_{i=1}^{3}\overline{Nu_i}\right)/3. \end{aligned}\right\} \tag{11}$$

2.2. Boundary conditions

$$\left.\begin{aligned} &\text{At } X=0: && U=\frac{\partial V}{\partial X}=\frac{\partial W}{\partial X}=0, \quad \frac{\partial\theta}{\partial X}=0.\\ &\text{At } X=2.25: && U=V=W=0, \quad \frac{\partial\theta}{\partial X}=0.\\ &\text{At } Y=0: && U=V=W=0,\\ & && \frac{\partial\theta}{\partial Y}=-1,\\ &\quad\text{for the iso-flux region (heaters),} && \\ & && \frac{\partial\theta}{\partial Y}=0,\\ &\quad\text{for the adiabatic region (the rest).} && \\ &\text{At } Y=1: && U=V=W=0, \theta=0.\\ &\text{At } Z=0 \text{ and } Z=7.5: && U=V=W=0, \quad \frac{\partial\theta}{\partial Z}=0. \end{aligned}\right\} \tag{12}$$

The numerical procedures are the same as reported previously [12]. Under-relaxation is used to ensure convergence, especially in the horizontal orientation and at higher Ra^*. As mentioned in [12], for validation of present program, the difference between present numerical results and results of Heindel et al. [7,8] is less than 4.5% in the range of $10^5 \leqslant Ra^* \leqslant 10^8$. In this paper, the range of Ra^* extends to as low as 10^2. However, finer grid $60\times30\times120$ is necessary due to the complex flow fields for inclined angle ϕ changing from 135° to 180° while grid $40\times20\times80$ is used for ϕ varying from 0° to 135°. Grid independence checks are carried out in three orientations ($\phi = 0°$, 90°, 180°) with 1.5 times finer grid, requiring more than one week of computational time in the SGI ORIGIAN 2000 work station.

3. Experimental setup

The experimental setup, shown schematically in Fig. 2(a), consists of a test cell, test bed and associated instruments for system control and collecting of data. The test cell, shown in Fig. 2(b), consists of a substrate plate, an opposing isothermal cooling wall, a side wall, two drive walls and a cover board compressed between two clamping plates by 4 bolts passing through each corner. The material of the substrate plate is Teflon, for strength at the experimental temperature, and the low thermal conductivity ($k = 0.35$ W/m K) acts as an insulation substrate plate. The substrate plate provides a support for holding a 3×3 array of 12.7 mm×12.7 mm×9 mm oxygen-free copper blocks spaced at 3.2 mm apart. To provide heating to each block, a thin square plate resistive heater (12 mm×12 mm×2 mm) is soldered to each block. The heater wall and side walls are bonded with sponge, an insulating material ($k = 0.038$ W/m K) to reduce possible heat loss, as shown in Fig.

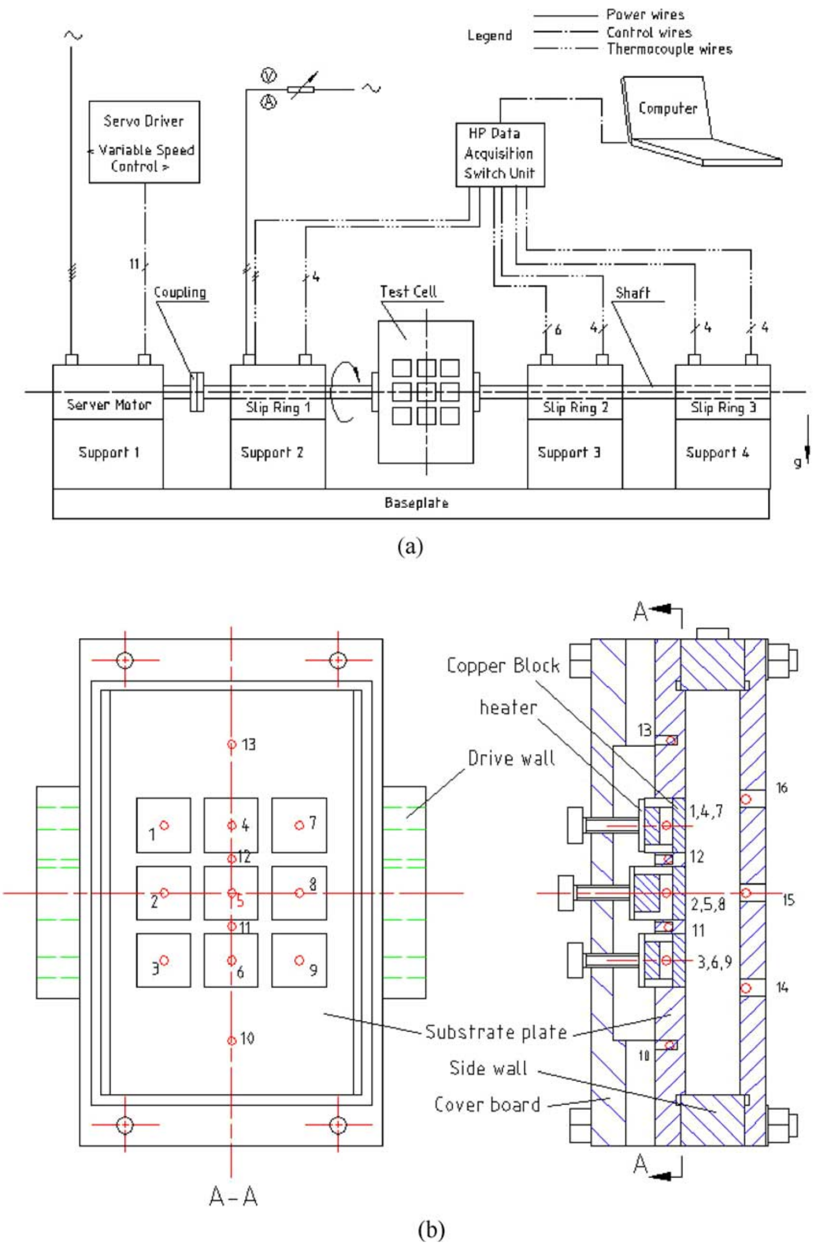

Fig. 2. The experimental setup: (a) schematic diagram of the experimental facility; (b) arrangement of the thermocouples.

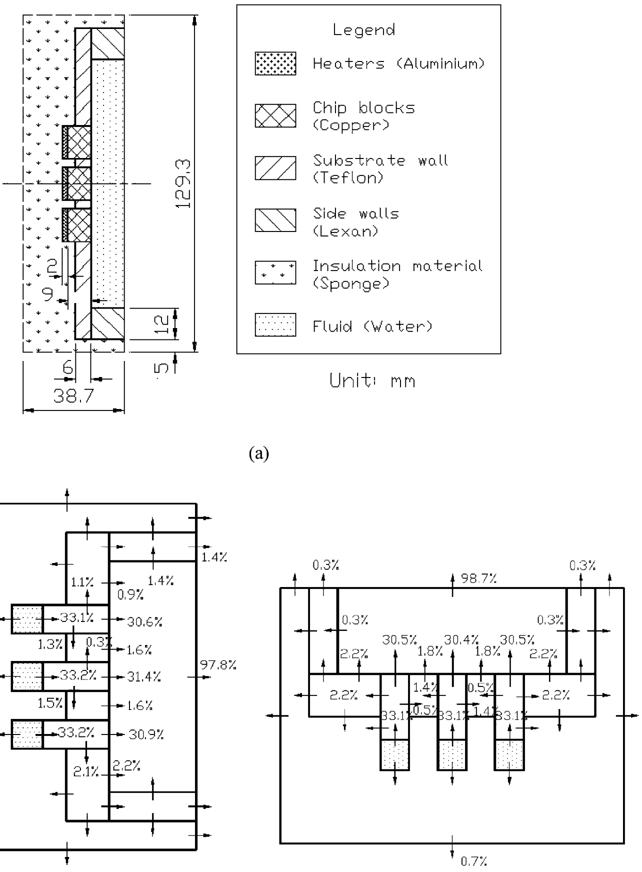

Fig. 3. Diagram of heat dissipation ($q''' = 5 \times 10^6$ W/m^3, $T_c = 20$ °C, $Ra \approx 1.222 \times 10^6$). (a) Model for experimental heat dissipation analysis; (b) heat dissipation $\phi = 90°$ and 180°.

3(a). The side wall is made of Lexan, a transparent material with low thermal conductivity ($k = 0.2$ W/m K). The isothermal cooling wall is made of copper with a high thermal conductivity ($k = 387.6$ W/m K), to provide a near uniform plate surface temperature. A fan is used to enhance convection heat transfer between the cooling wall and the environment to keep a constant temperature. Fig. 2(b) shows the thermocouples arrangement. The back of each copper block is instrumented with one K-type thermocouple located in holes drilled from the front surface of the block. The cooling wall surface temperature is measured via three surface-mounted thermocouples.

Experiments are conducted with degassed, deionized water. All heaters are equally powered, and steady-state temperature and power inputs are recorded by an HP data acquisition system interfaced to a PC. The test cavity can be kept at any prescribed angle using a universal protractor and balance. Fig. 3(a) shows the geometrical parameters and materials used for conjugate heat loss analysis. The contact thermal resistances between each surface are neglected. The heat transfer coefficient (h) is assumed 10 W/m^2 K for the boundary condition between sponge and environment. The results are not sensitive when h varied from 5 to 30 W/m^2 K. Fig. 3(b) shows the estimated heat distribution in the vertical orientation and the horizontal orientation (heated from below). The values of some heat transfer paths (arrows) are not given because they are less than 0.5%. In general, calculations show that more than 90 percent of the heat generated by heaters is dissipated through water and heat loss from the sponge, bottom wall and top wall is small (about 2%). Based on conjugate calculations, the conjugate correction factors ranged from 0.8 to 0.92 are used in data reduction. The method is described in [7,8]. The overall uncertainty in the Nusselt (Nu) and Rayleigh numbers (Ra^*) varied with the power input levels, with maximum uncertainties in Nu and Ra^* estimated to be 11% and 7%, respectively.

4. Results and discussions

4.1. Experimental results and numerical validation

Fig. 4 shows the comparison between numerical simulations ($1 \times 10^2 \leqslant Ra^* \leqslant \times 10^8$, $Pr = 5$, 9) and experimental data ($8 \times 10^5 \leqslant Ra^* \leqslant \times 10^8$, $Pr \approx 5$). In the experiments, the heaters in the same row have about the same temperature, probably due to the weak velocity in the horizontal direction in different inclined positions. This shows that the temperature distribution is symmetric in the X-direction. Since column-to-column variations are insignificant, row averaged $\overline{Nu}$ can be used without any loss of generality. (This phenomena is also proved by present numerical simulations and reported by experimental study of Polentini et al. [13] in the angular position of 90°, 120°, 135°, 150° and 180° for water and FC-77.) Better agreement is obtained for the middle row of heaters and the maximum differences between numerical simulations and experiment data are about 9%. In fact, the maximum differences take place in the bottom row of heaters. The temperature increases for the bottom row of heaters are smallest and are more sensitive to the conjugate effect and heat loss that is difficult to evaluate accurately due to the complex geometrical structure and thermal contact resistances.

4.2. Effect of inclination to flow pattern evolution

For all cases of numerical results, $\overline{Nu}$ generally reduces to about 1.5, as Ra^* decreases to its low limit of 100, which is less than the critical value of 1708. Theoretically, $\overline{Nu}$ assumes 1 for pure conduction with Ra^* approaches zero. In this conduction regime, $\overline{Nu}$ remains essentially unaltered until Ra^* approaches the lower critical value of 1708. As Ra^* passes the critical value there is clearly a sharp increase in heat transfer rate. The slopes of the curves change from zero to positive values. The increase in heat transfer rate is accomplished with the onset of natural convection.

In general, it is observed that there is a flow pattern evolution with inclined angle and Ra^*, as shown in Table 2. When the hot wall is on the top of the cold wall ($\phi = 0°$), even though the flow field looks complex and has the multi-cellular form, the velocity magnitude is so small ($\sim 1 \times 10^{-3}$ m/s) that it could not affect the temperature field. As a result, conduction heat transfer in the liquid coolant dominates, as shown in Fig. 5(a). It is

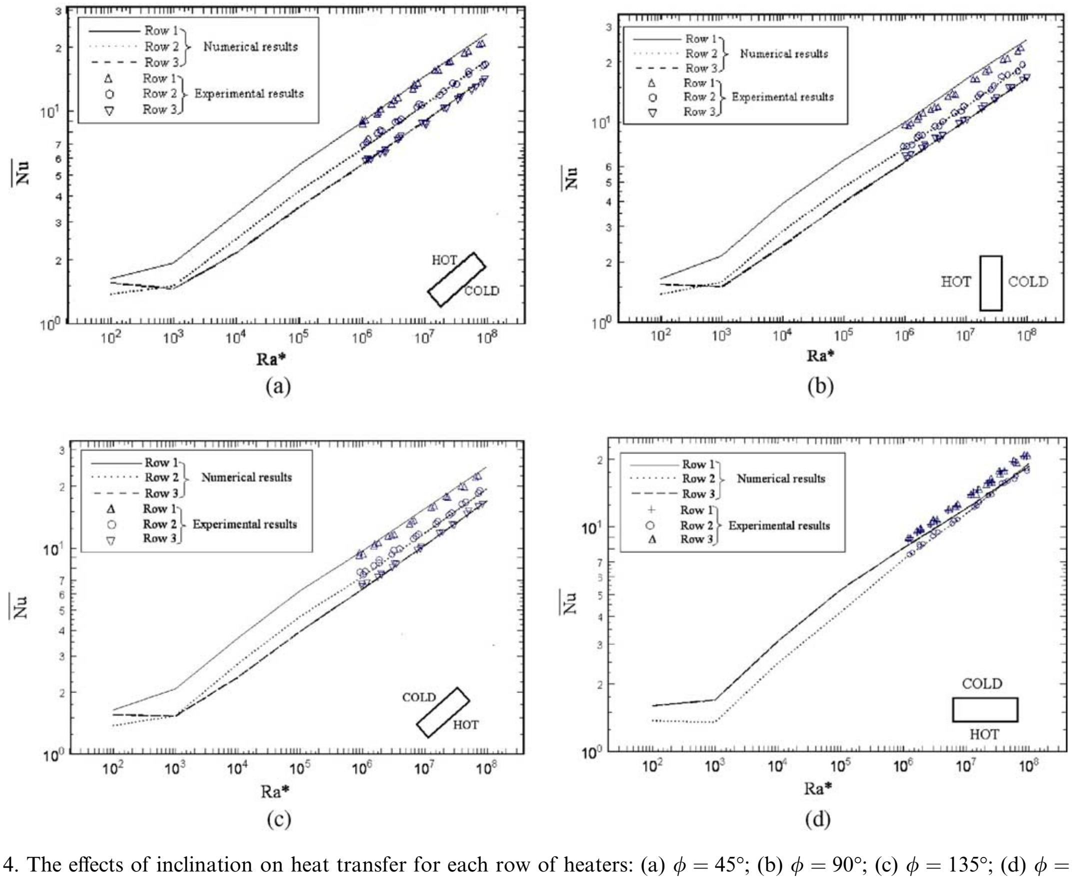

(a) (b) (c) (d)

Fig. 4. The effects of inclination on heat transfer for each row of heaters: (a) $\phi = 45°$; (b) $\phi = 90°$; (c) $\phi = 135°$; (d) $\phi = 180°$.

Table 2
Flow pattern evolution for water ($Pr \approx 5$)

ϕ	Ra^*
	Flow pattern evolution $Ra^* \approx 4.6 \times 10^5 \rightarrow 4.5 \times 10^6 \rightarrow 2.5 \times 10^7$
0°	Multi-cellular flow pattern, conduction heat transfer (Fig. 5(a))
↓	
90°	Uni-cellular boundary layer convection (Fig. 5(b))
↓	
150°	Multi-cellular convection (Fig. 5(c))
↓	
180°	Toroidal convection → Bimodal convection → R–B convection (Fig. 6(a)) (Fig. 6(b)) (Fig. 6(c))

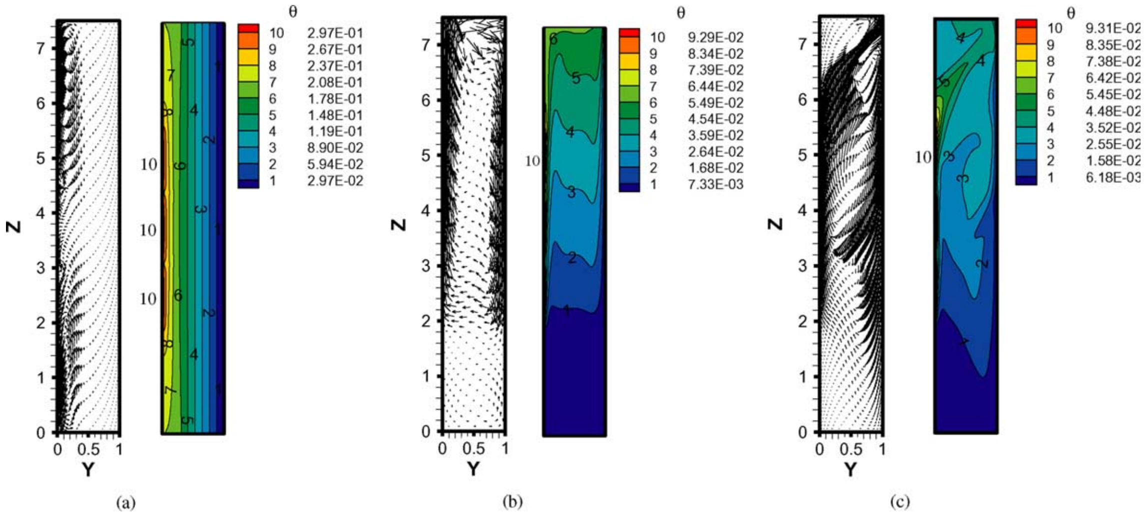

Fig. 5. Flow and temperature fields on Y–Z planes at $X = 0$ for water at different angular positions: (a) $\phi = 0°$, $Ra^* = 1.1 \times 10^7$; (b) $\phi = 90°$, $Ra^* = 1.1 \times 10^7$; (c) $\phi = 150°$, $Ra^* = 1.1 \times 10^7$.

known that two flow patterns, two-dimensional uni-cellular and three-dimensional multi-cellular flow patterns exist, when the inclined angle increases from the vertical orientation ($\phi = 90°$) to the horizontal orientation ($\phi = 180°$), as shown in Fig. 5. However, in the horizontal orientation, there is a complex flow pattern evolution which, to the authors' knowledge, has not been reported before.

In the low Ra^*, toroidal convection takes places, as shown in Figs. 6(a) and 7(a). (The scale of Fig. 6 corresponds to dimensionless velocity magnitude.) The hot fluid rises in the central region as a result of buoyancy forces, until it reaches near the top cold wall where it turns radially outward, towards the sidewalls while it is cooled. Then it turns downward near those walls. Finally, the restriction imposed by the bottom wall (substrate wall) forces the fluid to turn radially inward, receiving heat when it passes above the discrete heat sources. The flow path is completed as the colder fluid is entrained to the ascending flow at the center of the enclosure. The maximum velocity appears in the upper section of the center heater. Compared with other flow patterns, Toroidal convection is deleterious to heat transfer due to the high peak temperature in the center heater. However, in these Ra^* ranges for water, even though there is obvious difference in Nu as shown in Fig. 4(d), the difference in temperature for each heater is small ($\Delta T < 1$ °C). The flow field is so weak that it could not affect the temperature field greatly. As a result, it is found that the all nine heaters almost keep to the same average temperature in the experiment. Sezai and Mohamad studied the flow pattern with a single heat source for air and discussed only the toroidal convection [14].

With increasing Ra^*, bimodal convection occurs, as shown in Figs. 6(b) and 7(b). In general, the flow pattern consists of two rolls rotating clockwise at the short side of the enclosure, with the warm up-streams of the two rolls mixing above the middle row of heaters. Near the

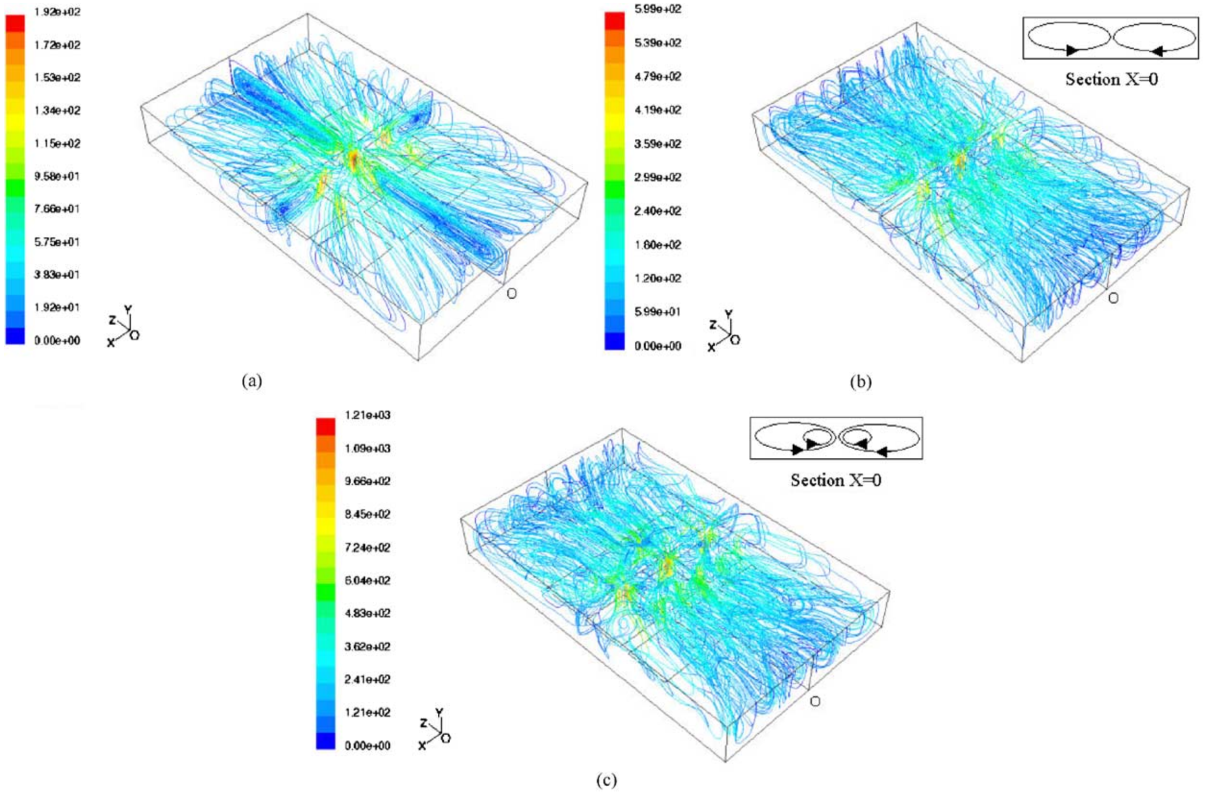

Fig. 6. Flow pattern evolution in the horizontal orientation ($\phi = 180°$): (a) toroidal convection $Ra^* \approx 4.6 \times 10^5$, $\phi = 180°$; (b) bimodal convection $Ra^* \approx 4.5 \times 10^6$, $\phi = 180°$; (c) R–B convection $Ra^* \approx 2.5 \times 10^7$, $\phi = 180°$.

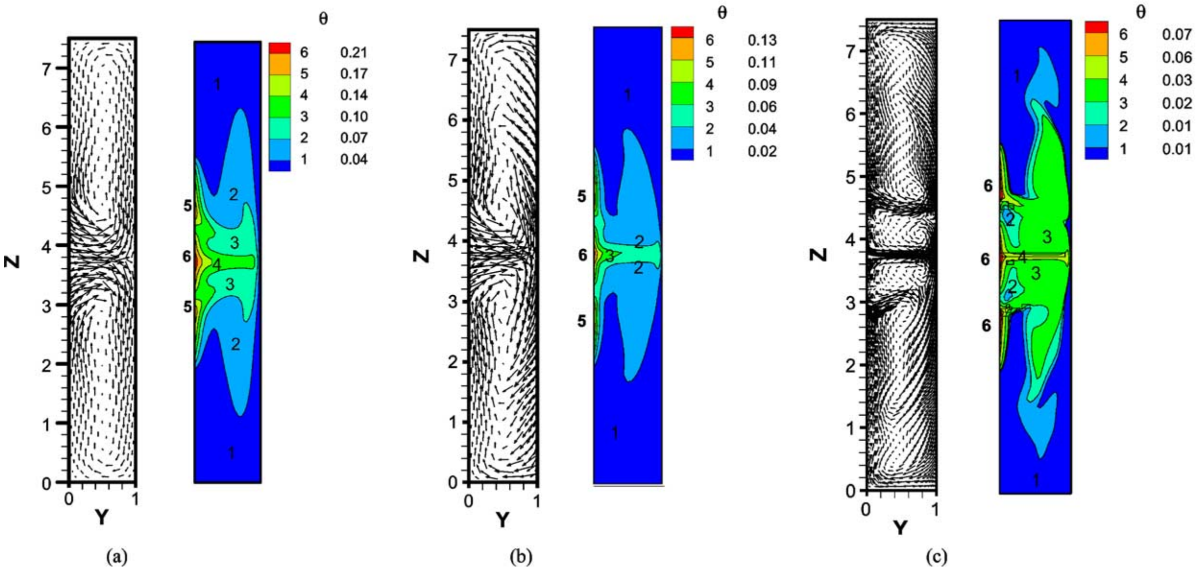

Fig. 7. Flow and temperature field for Y–Z planes at $X = 0$ for water in the horizontal orientation ($\phi = 180°$): (a) toroidal convection $Ra^* \approx 4.6 \times 10^5$; (b) bimodal convection $Ra^* \approx 4.5 \times 10^6$; (c) R–B convection $Ra^* \approx 2.5 \times 10^7$.

lateral wall, velocity in the X-direction is obvious, just as the case of toroidal convection. But in the central region, there is a 2-D bimodal convection dominating the flow reflecting a continuing evolution process. Bimodal convection is also reported by Mukutmoni and Yang [15] when studying the constant wall temperature problem in a shallow enclosure.

When Ra^* is high enough, R–B convection occurs, and takes the form of four-roll pattern, as seen in Figs. 6(c) and 7(c) (for $Ra^* \approx 2.5 \times 10^7$). In general, the paths of particles in Fig. 6(c) are parallel, reflecting weak movement in X-direction and the flow is close to 2-D, resulting in almost the same temperature in the same row of heaters. In Fig. 7(c), the two side rolls, due to transition effects, can be called developing R–B rolls here. With further increase in Ra^*, convection with more rolls are expected. According to Cole and Fernando [17], constant heat flux boundary condition makes cell patterns much faster than constant temperature boundary conditions. For constant wall temperature of the bottom boundary, the flow appears to become turbulent for $Ra > 1.6 \times 10^4\ Pr^{1.4}$ while $Ra^* > 10^8$ for constant heat flux bottom boundary. Experimental studies of Polentini et al. [13] showed laminar flow even in $Ra^* \approx 4.6 \times 10^8$, which supports our laminar flow assumption.

4.3. Effect of inclination to distortion of temperature field

When the inclined angle approaches the horizontal orientation ($\phi = 180°$), distortion in temperature field begins to appear, and intensify at the top rows of heaters as shown in Fig. 8. This greatly enhances heat transfer for the top row of heaters. From the vector plot in Figs. 9 and 10, the distorted temperature fields could be explained as follows. In the vertical orientation, from the fringe to the heater, there is a sharp velocity increase. But at the heater, the velocity magnitude remains constant. From mass continuity, some fluid is pushed from the fringe to the heater. There is thus span-wise motion even though it is weak. But at the heater, no such span-wise motion exists, due to more uniform velocity magnitude. However, in the inclined orientation, even at the heaters the velocity profile shows two peaks. Correspondingly, there are two local high temperature regions at the heaters, resulting in temperature field distortion (Fig. 8(b)). This trend is intensified with increasing Ra^* or with greater deviation from the vertical orientation to the horizontal orientation, resulted from a stronger x-velocity, with transition from 2-D flow pattern to a 3-D one.

4.4. Effect of inclination to local heat transfer rate

Fig. 11 shows the local Nu distributions along different lines at the heater plate. To distinguish each other, the edge effect for $X = \pm 1.75$ is called remote edge effect while the edge effect for $X = \pm 0.5$ is called the inner edge effect. In Fig. 11(a), for conduction heat transfer at $\phi = 0°$, edge effects are mild compared with convection heat transfer. The difference between different rows of heaters is small. In Fig. 11(b), at vertical orientation, the bottom row of heaters has the highest Nu and the edge effect clearly increases heat transfer. This explains why the results of 2-D model with neglected edge effects are 20% lower compared to that of 3-D model [7]. In this flow pattern model, remote edge effect is near to the

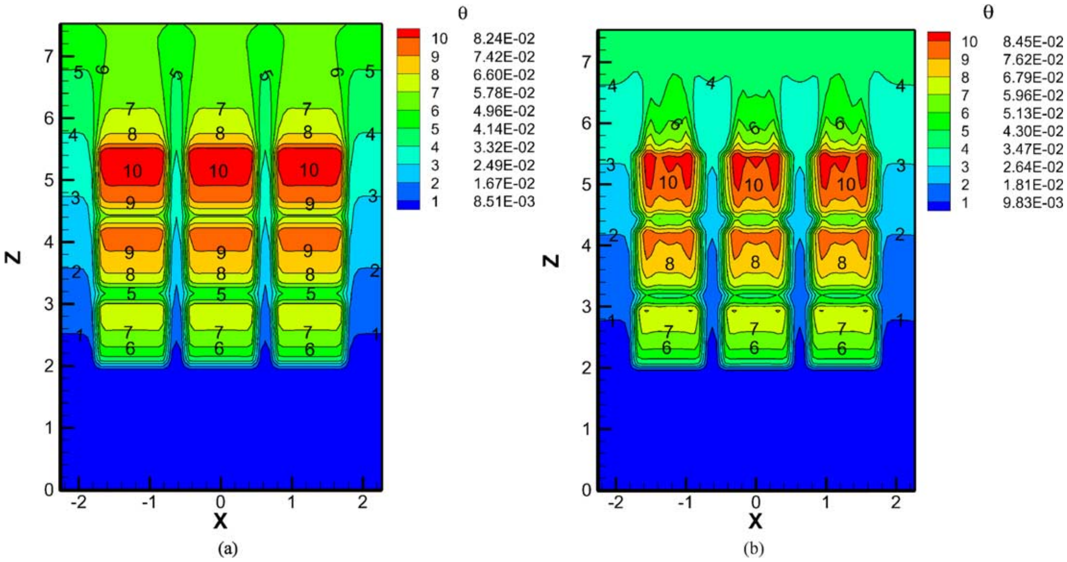

Fig. 8. Temperature distortion for water at different inclined angles ($Ra^* \approx 2.5 \times 10^7$): (a) $\phi = 90°$; (b) $\phi = 135°$.

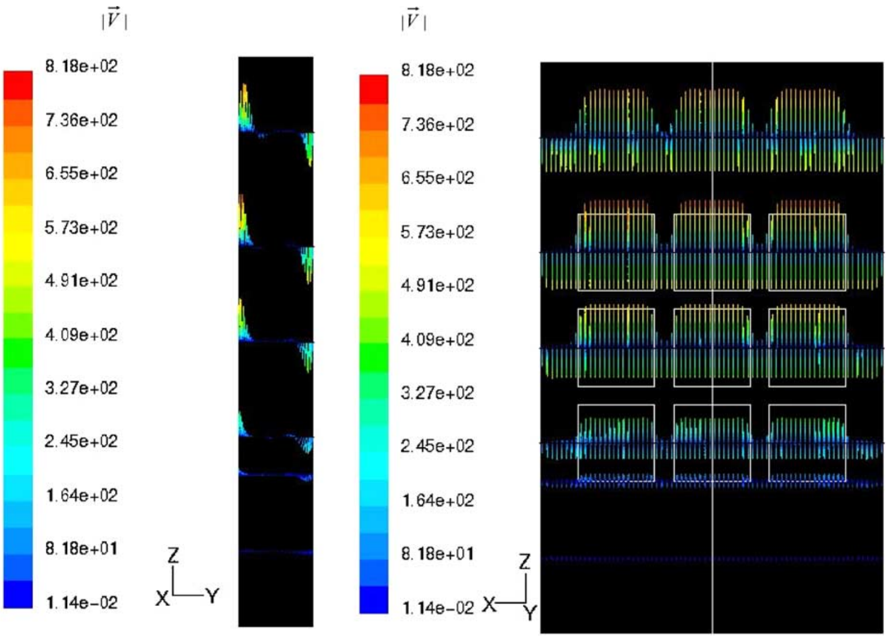

Fig. 9. Vector plot for water at selected $Z = 1, 2, 2.5, 3.75, 5, 6.5$ planes ($Ra^* \approx 2.5 \times 10^7$, $\phi = 90°$).

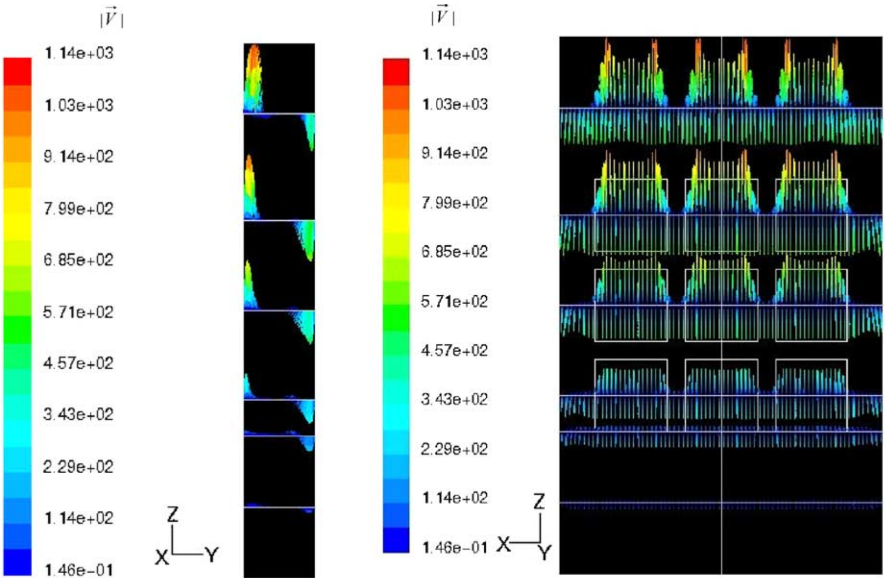

Fig. 10. Vector plot for water at selected $Z = 1, 2, 2.5, 3.75, 5, 6.5$ planes ($Ra^* \approx 2.5 \times 10^7$, $\phi = 120°$).

inner edge effect, due to the weak velocity in the X-direction.

Similar to previous discussion, Fig. 11(c) shows that Nu reduces from the bottom row of heaters to the top row. Heat transfer for the bottom row becomes worse. However, heat transfer of the top row, which has the maximum temperature of the enclosure and determines the heat transfer capability, is improved. It is more obvious in the horizontal orientation, as shown in Fig. 11(d), where, because the lowest $\overline{Nu}$ among the three rows, is higher than those of other orientations. Thus, the horizontal orientation is best for heat transfer.

From Fig. 11, we find that there is a clear difference between remote edge effect and inner edge effect for 3-D

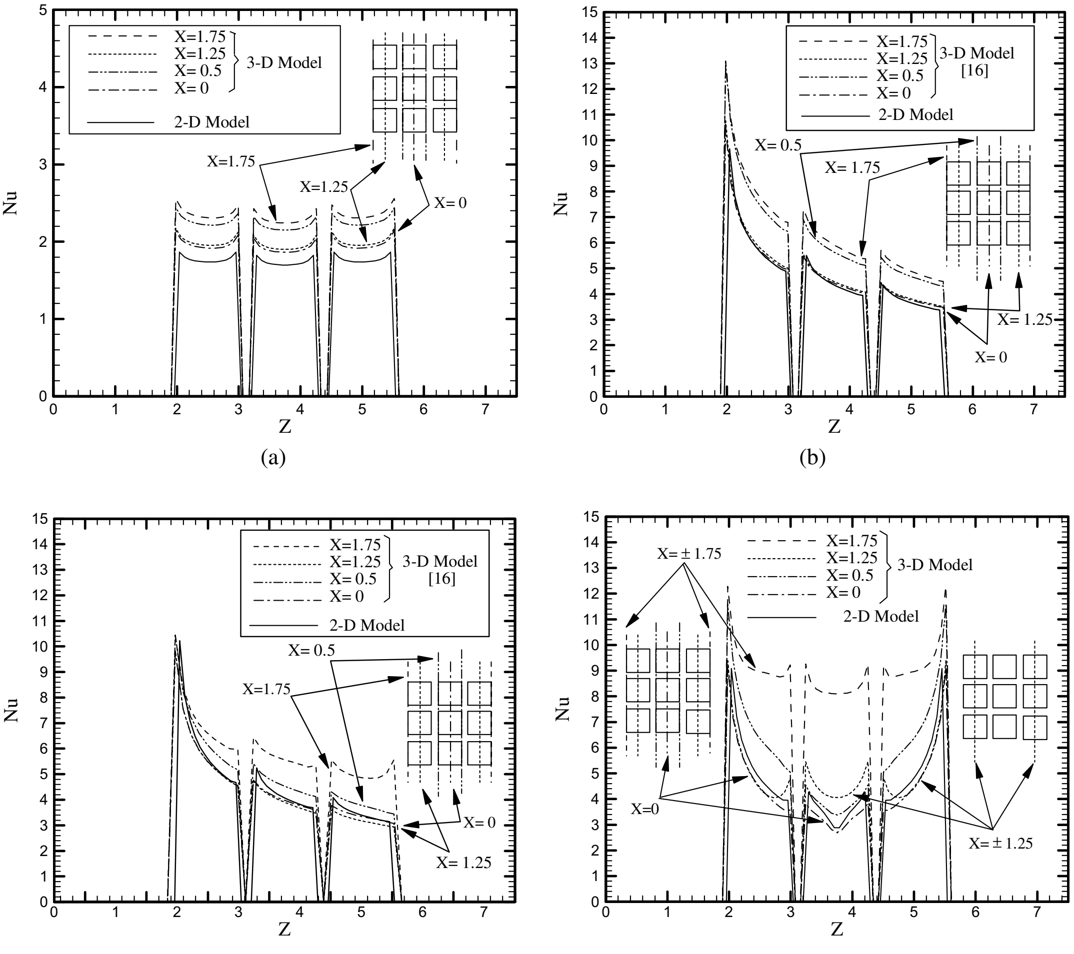

(a) (b) (c) (d)

Fig. 11. Local Nusselt number distribution for water at different inclined angles ($Ra^* = 1 \times 10^5$, $Pr = 5$): (a) $\phi = 0°$; (b) $\phi = 90°$; (c) $\phi = 150°$; (d) $\phi = 180°$.

results. However, there are only small differences in the local *Nu* distribution along the center lines of the three column of heaters. As seen in Fig. 11, they are also close to the 2-D results for all inclined angular positions. Therefore, when *Pr* is discussed in next section, 2-D model can be used without losing generality.

4.5. Effects of Prandtl number

Present results of 3-D numerical simulations in vertical orientation are showed in Fig. 12. In addition, computations are carried out for various fluids ($Pr = 0.7,\ 5,\ 20,\ 120$) in all inclined angles ($\phi = 0° \sim 180°$) for 2-D modeling, as shown in Fig. 13. It is found that, with other parameters unaltered, the effects of *Pr* are (i) for most liquids (except metal liquids), whose *Pr* is greater than 1, the effects of *Pr* are negligible, and (ii) for most gases whose *Pr* are about 0.7, the effects of *Pr* are small and the differences between liquids and gases in $\overline{Nu}$ and $\overline{\overline{Nu}}$ are small.

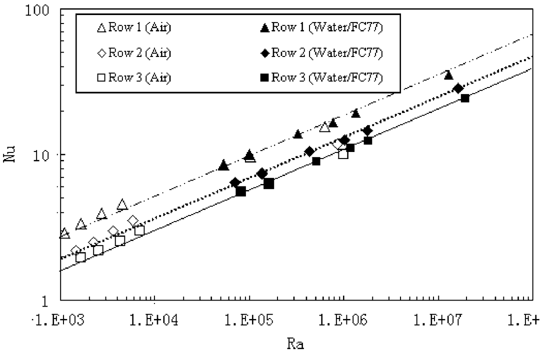

Fig. 12. The effects of Prandtl number in vertical orientation from 3-D numerical simulations.

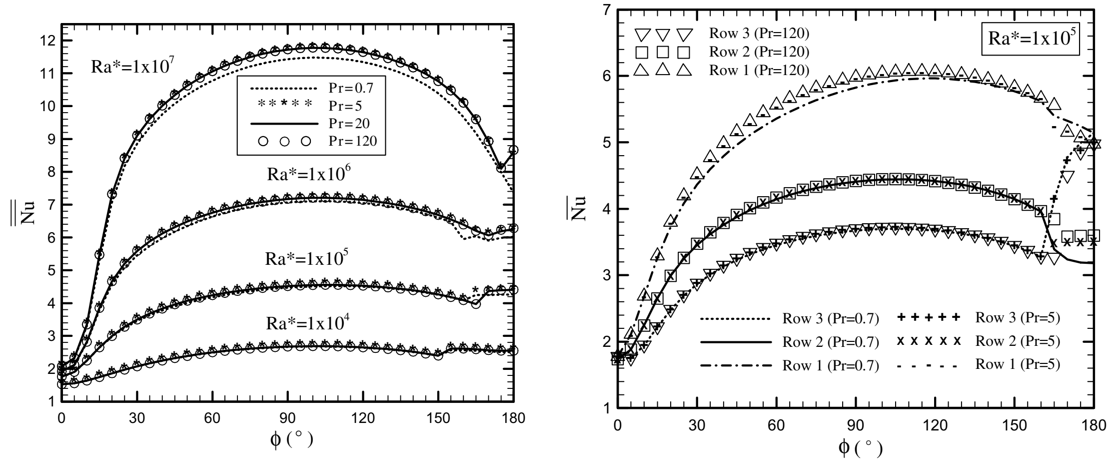

(a) (b)

Fig. 13. The effects of Prandtl number in different orientations from 2-D numerical simulations: (a) at different Rayleigh number; (b) at different rows.

In fact, the experimental study of Polentini et al. [13] showed that water ($Pr \approx 5$) and FC-77 ($Pr \approx 25$) obey the same empirical correlations from the vertical orientation ($\phi = 90°$) to the horizontal orientation ($\phi = 180°$). The effect of Pr in the vertical orientation and horizontal orientation (heated from below) for non-discrete heat sources has been studied by others [12,18,19]. The follow equations are given by Berkovsky and Polevikov (from [18]), Bejan [18], Globe and Dropkin [19], respectively, to describe the effect of Pr.

$$g(Pr) = (Pr + 0.2)^{0.28} \quad (Pr < 10^5, Ra < 10^{13}, \phi = 90°), \tag{13}$$

$$g(Pr) = \begin{cases} Pr^{0.25} & (Pr < 1) \\ 1 & (Pr \geqslant 1) \end{cases}$$
$$\text{(For boundary layerflow and } \phi = 90°\text{)}, \tag{14}$$

$$g(Pr) = Pr^{0.074}$$
$$(0.02 \leqslant Pr \leqslant 8750, 1.51 \times 10^5 \leqslant Ra \leqslant 6.76 \times 10^8, \phi = 180°), \tag{15}$$

where $g(Pr)$ is a function of Pr.

Present studies are comparable with the above equations as they are all weak functions of Pr. In particular, Eq. (14) is derived from scale analysis based on the assumption that the buoyancy force is balanced by friction force (for $Pr \gg 1$) or inertial force (for $Pr \ll 1$) in vertical orientation [18]. Because this assumption can be applied to all inclined orientations for natural convection, perhaps this equation may be applicable to all orientations to give an estimate for heat transfer that may be useful for new coolants.

5. Conclusions

The main conclusions are:

(1) An experimental study is carried out to study natural convection in a cavity with discrete heat sources at various orientations. In general, heaters in the same row have almost the same temperature, due to weak velocity in the horizontal direction.
(2) In-depth 2-D and 3-D numerical simulations for laminar flow are implemented and compared with experimental results. Complex flow pattern evolution, flow field, and temperature fields are observed due to interactions of buoyancy forces tangential and normal to the heater surfaces.
(3) In the horizontal orientation, with the increasing of Ra^*, the flow pattern evolutions are complex and identified with three main characteristics: from toroidal convection to bimodal convection to R–B convection. For increase heat transfer, the horizontal orientation is best because the lowest $\overline{Nu}$ among the three rows is higher than those of other orientations.
(4) On inclining the enclosure toward the horizontal orientation (heated from below), the flow and temperature fields become complex and distorted. Three-dimensional effects, such as fluid flow in horizontal direction and distorted temperature field begin to appear and intensify, which greatly enhance the heat transfer for the top row.
(5) Edge effect increases heat transfer greatly. Without edge effects, the results of 2-D model are close to those of 3-D model.
(6) For most liquids (except metal liquids), whose Pr is greater than 1, the effects of Pr are negligible, and

for most gases whose *Pr* are about 0.7, the effects of *Pr* are small and the differences between liquids and gases in $\overline{Nu}$ and $\overline{\overline{Nu}}$ are small.

References

[1] L.T. Yeh, Review of heat transfer technologies in electronic equipment, J. Electron. Packaging 117 (1995) 333–339.

[2] F.P. Incropera, Convection heat transfer in electronic equipment, J. Heat Transfer 110 (1988) 1097–1111.

[3] I. Mudawar, Direct-immersion cooling for high power electronic chips, in: Proceedings of I-Therm III: Intersociety Conference on Thermal Phenomena in Electronic Systems, Austin, Texas, USA, 1992, pp. 74–84.

[4] D. Wroblewski, Y. Joshi, Computations of liquid immersion cooling for a protruding heat source in a cubical enclosure, Int. J. Heat Mass Transfer 36 (1993) 1201–1218.

[5] D. Wroblewski, Y. Joshi, liquid immersion cooling of a substrate-mounted protrusion in a three-dimensional enclosure: the effects of geometry and boundary conditions, J. Heat Transfer 116 (1994) 112–119.

[6] D. Mukutmoni, Y.K. Joshi, M.D. Kelleher, Computations for a three-by-three array of protrusions cooled by liquid immersion: effect of thermal conductivity, Adv. Electron. Packaging ASME EEP 42 (1993) 745–753.

[7] T.J. Heindel, S. Ramadhyani, F.P. Incropera, Laminar natural convection in a discretely heated cavity. I. Assessment of three-dimensional effects, J. Heat Transfer 117 (1995) 902–909.

[8] T.J. Heindel, F.P. Incropera, S. Ramadhyani, Laminar natural convection in a discretely heated cavity. II. Comparisons of experimental and theoretical results, J. Heat Transfer 117 (1995) 910–917.

[9] T.J. Heindel, S. Ramadhyani, F.P. Incropera, Conjugate natural convection from an array of discrete heat sources. Part 1—two- and three-dimensional model validation, Int. J. Heat Fluid Flow 16 (1995) 501–510.

[10] T.J. Heindel, F.P. Incropera, S. Ramadhyani, Conjugate natural convection from an array of discrete heat sources. Part 2—a numerical parametric study, Int. J. Heat Fluid Flow 16 (1995) 511–518.

[11] F.P. Incropera, Liquid cooling of electronic devices by single-phase convection, in: Wiley Series in Thermal Management of Microelectronic and Electronic Systems, 1999, pp. 90–124.

[12] S.K.W. Tou, C.P. Tso, X. Zhang, 3-D numerical analysis of natural convective liquid cooling of a 3×3 heater array in rectangular enclosure, Int. J. Heat Mass Transfer 42 (1999) 3231–3244.

[13] M.S. Polentini, S. Ramadhyani, F.P. Incropera, Single phase thermosyphon cooling of an array of discrete heat sources in a rectangular cavity, Int. J. Heat Mass Transfer 36 (1993) 3983–3996.

[14] I. Sezai, A.A. Mohamad, Natural convection from a discrete heat source on the bottom of a horizontal enclosure, Int. J. Heat Mass Transfer 36 (2000) 2257–2266.

[15] D. Mukutmoni, K.T. Yang, Rayleigh–Benard convection in a small aspect ratio enclosure. Part I—bifurcation to oscillatory convection, J. Heat Transfer 115 (1993) 360–366.

[16] S.K.W. Tou, X.F. Zhang, Three-dimensional numerical simulation of natural convection in an inclined liquid-filled enclosure with an array of discrete heaters, Int. J. Heat Mass Transfer 46 (2003) 127–138.

[17] G.S. Cole, H.J.S. Fernando, Some aspects of the decay of convective turbulence, Fluid Dyn. Res. 23 (1998) 161–176.

[18] A. Bejan, Convection Heat Transfer, second ed., Wiley, New York, 1995, pp. 243–247.

[19] S. Globe, D. Dropkin, Natural convection heat transfer in liquids confined by two horizontal plates and heated from below, J. Heat Transfer 81 (1959) 24–28.